3

A Class-F_3 CMOS Oscillator

An oscillator topology demonstrating an improved phase noise performance is introduced and analyzed in this chapter. It exploits a time-variant phase noise model with insights into the phase noise conversion mechanisms. This oscillator enforces a pseudo-square voltage waveform around the LC tank by increasing the third harmonic of the fundamental oscillation voltage through an additional impedance peak. This auxiliary impedance peak is realized by a transformer with moderately coupled resonating windings. As a result, the effective impulse sensitivity function (ISF) decreases, thus reducing the oscillator's effective noise factor such that a significant improvement in the oscillator phase noise and power efficiency is achieved. A comprehensive study of circuit-to-phase-noise conversion mechanisms of different oscillators' structures shows that the class-F_3 exhibits the lowest phase noise at the same tank's quality factor and supply voltage. The prototype of the class-F_3 oscillator is implemented in TSMC 65-nm standard CMOS. It exhibits average phase noise of -142 dBc/Hz at 3 MHz offset from the carrier over 5.9–7.6 GHz tuning range with figure of merit of 192 dBc/Hz. The oscillator occupies 0.12 mm^2 while drawing 12 mA from 1.25 V supply.

3.1 Introduction

Designing voltage-controlled and digitally controlled oscillators (VCO, DCO) of high spectral purity and low power consumption is quite challenging, especially for GSM transmitter (TX), where the oscillator phase noise must be less than -162 dBc/Hz at 20 MHz offset frequency from 915 MHz carrier [1]. At the same time, the RF oscillator consumes disproportionate amount of power of an RF frequency synthesizer [2, 3] and burns more than 30% of the cellular RX power [4, 5]. Consequently, any power reduction of RF oscillators will greatly benefit the overall transceiver power efficiency and

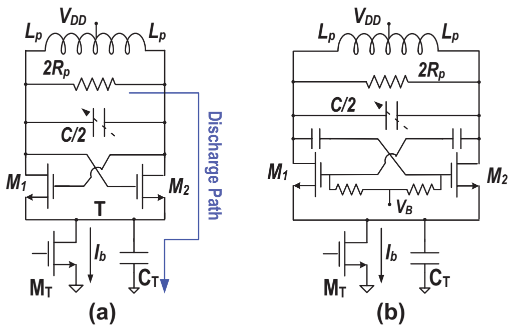

Figure 3.1 Oscillator schematic: (a) traditional class-B; (b) class-C.

ultimately the battery lifetime. This motivation has encouraged an intensive research to improve the power efficiency of an RF oscillator while satisfying the strict phase noise requirements of the cellular standards.

The traditional class-B oscillator (Figure 3.1(a)) is the most prevalent architecture due to its simplicity and robustness. However, as shown in Chapter 2, its phase noise and power efficiency performance drops dramatically by replacing the ideal current source with a real one. For the best performance, the oscillation amplitude should be near supply voltage V_{DD} [6, 7]. Therefore, the gm-devices $M_{1/2}$ enter deep triode for part of the oscillation period. The low impedance path between node "T" due to M_T together with $M_{1/2}$ entering deep triode degrades Q-factor of the tank dramatically and phase noise improvement by increasing oscillation voltage would be negligible.

The noise filtering technique [8] provides a relatively high impedance between the gm-devices and the current source. Hence, the structure maintains the intrinsic Q-factor of the tank during the entire oscillation period. However, it requires an extra resonator sensitive to parasitic capacitances, increasing the design complexity, area, and cost.

As we discussed in Chapter 2, the class-C oscillator (Figure 3.1(b)) prevents the gm-devices from entering the triode region [9, 10]. Hence, the tank Q-factor is preserved throughout the oscillation period. By changing the drain current shape to the "tall and narrow" form for the class-C operation, the oscillator saves 36% power. However, the constraint of avoiding entering the triode region limits the maximum oscillation amplitude of the class-C oscillator to around $V_{DD}/2$, for the case of bias voltage V_B as low as a threshold voltage of the active devices, which limits the lowest achievable phase noise performance.

Harmonic tuning oscillator enforces a pseudo-square voltage waveform around the LC tank through increasing the third harmonic component of the fundamental oscillation voltage through an additional tank impedance peak at that frequency. Kim et al. [11] exploited this technique to improve the phase noise performance of the LC oscillator by increasing the oscillation zero-crossings' slope. However, that structure requires more than two separate LC resonators to make the desired tank input impedance. It increases die area and cost and decreases tuning range due to larger parasitics. Furthermore, the oscillator transconductance loop gain is the same for both resonant frequencies, thus raising the probability of undesired oscillation at the auxiliary tank input impedance. Here, we show how to resolve the concerns and quantify intuitively and theoretically the phase noise and power efficiency improvement of the class-F_3 oscillator compared to other structures [12, 13, 31].

The chapter is organized as follows: Section 3.2 establishes the environment to introduce the class-F_3 oscillator. The circuit-to-phase-noise conversion mechanisms are studied in Section 3.3. Section 3.4 presents extensive measurement results of the prototype, while Section 3.5 wraps up this chapter with conclusions.

3.2 Evolution Towards Class-F_3 Oscillator

Suppose the oscillation voltage around the tank was a square wave instead of a sinusoidal. As a consequence, the oscillator would exploit the special ISF [14] properties of the square-wave oscillation voltage to achieve a better phase noise and power efficiency. However, the gm-devices would work in the triode region (shaded area in Figure 3.2(b)) even longer than in the case

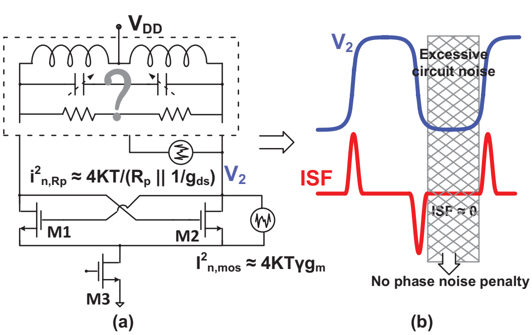

Figure 3.2 LC-tank oscillator: (a) noise sources; (b) targeted oscillation voltage (top) and its expected ISF (bottom).

of the sinusoidal oscillator. Hence, the loaded resonator and gm-device inject more noise to the tank. Nevertheless, ISF value is expected to be negligible in this time span due to the zero derivative of the oscillation voltage [14]. Although the circuit injects huge amount of noise to the tank, the noise cannot change the phase of the oscillation voltage and thus there is no phase noise degradation.

3.2.1 Realizing a Square Wave Across the LC Tank

The above reasoning indicates that the square-wave oscillation voltage has special ISF properties that are beneficial for the oscillator phase noise performance. But how can a square wave be realized across the tank? Let us take a closer look at the traditional oscillator in the frequency domain. As shown in Figure 3.3, the drain current of a typical LC-tank oscillator is approximately a square wave. Hence, it ideally has a fundamental and odd harmonic components. On the other hand, the tank input impedance has a magnitude peak only at the fundamental frequency. Therefore, the tank filters out the harmonic components of the drain current and finally a sinusoidal wave is seen across the tank.

Now, suppose the tank offers another input impedance magnitude peak around the third harmonic of the fundamental frequency (see Figure 3.4). The tank would be prevented from filtering out the third harmonic component of the drain current. Consequently, the oscillation voltage will contain a significant amount of the third harmonic component in addition to the fundamental:

$$V_{in} = V_{p1} \sin(\omega_0 t) + V_{p3} \sin(3\omega_0 t + \Delta\phi) \tag{3.1}$$

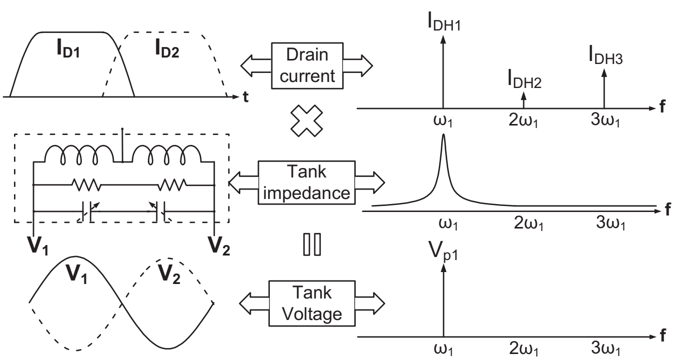

Figure 3.3 Traditional oscillator waveforms in time and frequency domains.

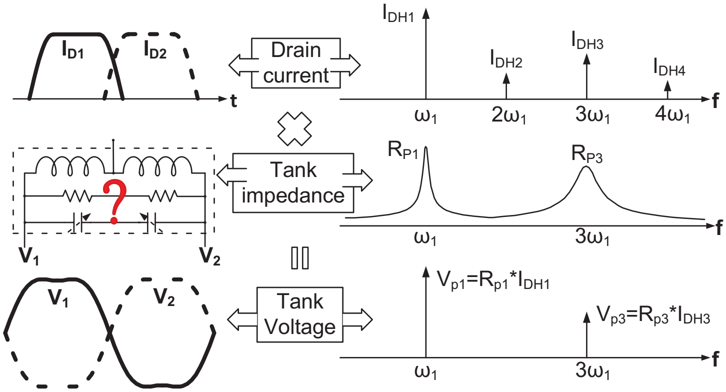

Figure 3.4 New oscillator's waveforms in time and frequency domains.

ζ is defined as the magnitude ratio of the third-to-first harmonic components of the oscillation voltage.

$$\zeta = \frac{V_{p3}}{V_{p1}} = \left(\frac{R_{p3}}{R_{p1}}\right)\left(\frac{I_{DH3}}{I_{DH1}}\right) \approx 0.33\left(\frac{R_{p3}}{R_{p1}}\right), \tag{3.2}$$

where R_{p1} and R_{p3} are the tank impedance magnitudes at the main resonant frequency ω_1 and $3\omega_1$, respectively. Figure 3.5 illustrates the oscillation voltage and its related expected ISF function (based on the closed-form equation in [14]) for different ζ values. The ISF rms value of the new oscillation waveform can be estimated by the following expression for $-\pi/8 < \Delta\phi < \pi/8$:

$$\Gamma_{rms}^2 = \frac{1}{2}\frac{1+9\zeta^2}{(1+3\zeta)^2}. \tag{3.3}$$

The waveform would become a sinusoidal for the extreme case of $\zeta = 0, \infty$, so (3.3) predicts $\Gamma_{rms}^2 = 1/2$, which is well known for the traditional oscillators. Γ_{rms}^2 reaches its lowest value of 1/4 for $\zeta = 1/3$, translated to a 3-dB phase noise and FoM improvement compared to the traditional oscillators. Furthermore, ISF of the new oscillator is negligible while the circuit injects significant amount of noise to the tank. Consequently, the oscillator FoM improvement could be larger than that predicted by just the ISF rms reduction.

3.2.2 F_3 Tank

The argumentation related to Figure 3.4 advocates the use of two resonant frequencies with a ratio of 3. The simplest way of realizing that would

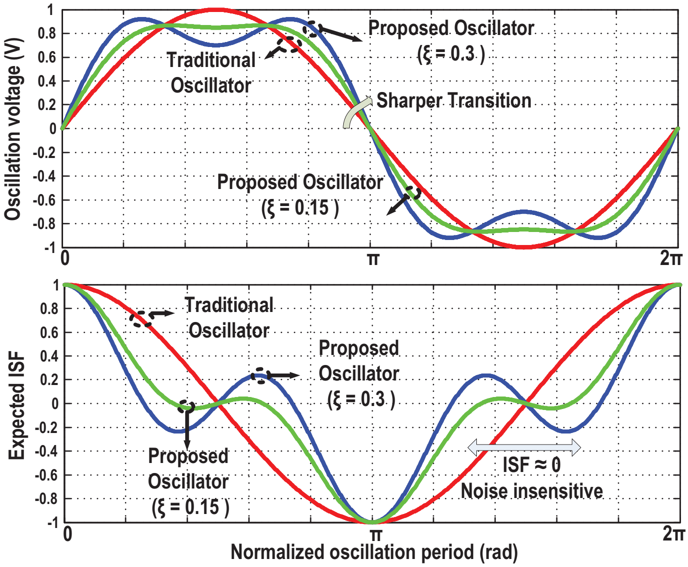

Figure 3.5 The effect of adding third harmonic in the oscillation waveform (top) and its expected ISF (bottom).

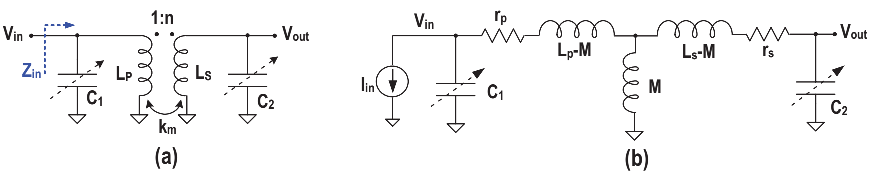

Figure 3.6 Transformer-based resonator (a) and its equivalent circuit (b).

be with two separate inductors [11, 15]. However, this will be bulky and inefficient. The chosen option in this work is a transformer-based resonator. The preferred resonator consists of a transformer with turns ratio n and tuning capacitors C_1 and C_2 at the transformer's primary and secondary windings, respectively (see Figure 3.6). Equation (3.4) expresses the exact mathematical equation of the input impedance of the tank.

$$Z_{in} = \frac{s^3\left(L_pL_sC_2\left(1-k_m^2\right)\right)+s^2(C_2(L_sr_p+L_pr_s))+s(L_p+r_sr_pC_2))+r_p}{\begin{array}{c}s^4\left(L_pL_sC_1C_2\left(1-k_m^2\right)\right)+s^3\left(C_1C_2\left(L_sr_p+L_pr_s\right)\right)+\\ s^2\left(L_pC_1+L_sC_2+r_pr_sC_1C_2\right)\right)+s\left(r_pC_1+r_sC_2\right)+1\end{array}}, \quad (3.4)$$

where k_m is the magnetic coupling factor of the transformer, r_p and r_s model the equivalent series resistance of the primary L_p and secondary L_s

inductances [16]. The denominator of Z_{in} is a fourth-order polynomial for the imperfect coupling factor (i.e., $k_m < 1$). Hence, the tank contains two different conjugate pole pairs, which realize two different resonant frequencies. Consequently, the input impedance has two magnitude peaks at these frequencies. Note that both resonant frequencies can satisfy the Barkhausen criterion with a sufficient loop gain [17]. However, the resulting multi-oscillation behavior is undesired and must be avoided [18]. In our case, it is preferred to see an oscillation at the lower resonant frequency ω_1 and the additional tank impedance at ω_2 is used to make a pseudo-square waveform across the tank. These two possible resonant frequencies can be expressed as

$$\omega_{1,2}^2 = \frac{1 + \left(\frac{L_s C_2}{L_p C_1}\right) \pm \sqrt{1 + \left(\frac{L_s C_2}{L_p C_1}\right)^2 + \left(\frac{L_s C_2}{L_p C_1}\right)\left(4k_m^2 - 2\right)}}{2 L_s C_2 \left(1 - k_m^2\right)}. \tag{3.5}$$

The following expression offers a good estimation of the main resonant frequency of the tank for $0.5 \leq k_m \leq 1$.

$$\omega_1^2 = \frac{1}{(L_p C_1 + L_s C_2)} \tag{3.6}$$

However, we are interested in the ratio of resonant frequencies as given by

$$\frac{\omega_2}{\omega_1} = \sqrt{\frac{1 + X + \sqrt{1 + X^2 + X\left(4k_m^2 - 2\right)}}{1 + X - \sqrt{1 + X^2 + X\left(4k_m^2 - 2\right)}}} \tag{3.7}$$

where X-factor is defined as

$$X = \left(\frac{L_s}{L_p} \cdot \frac{C_2}{C_1}\right). \tag{3.8}$$

Equation (3.7) indicates that the resonant frequency ratio ω_2/ω_1 is just a function of the transformer inductance ratio $\mathrm{L}_s/\mathrm{L}_p$, tuning capacitance ratio $\mathrm{C}_2/\mathrm{C}_1$, and transformer magnetic coupling factor k_m. The relative matching of capacitors (and inductors) in today's CMOS technology is expected to be much better than 1%, while the magnetic coupling is controlled through lithography that precisely sets the physical dimensions of the transformer. Consequently, the relative position of the resonant frequencies is not sensitive to the process variation. The ω_2/ω_1 ratio is illustrated versus X-factor for different k_m in Figure 3.7. As expected, the ratio moves to higher values for larger k_m and finally the second resonance disappears for the perfect coupling

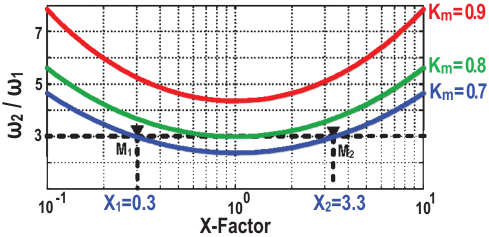

Figure 3.7 Ratio of the tank resonant frequencies versus X-factor for different k_m.

factor. The ratio of ω_2/ω_1 reaches the desired value of 3 at two points for the coupling factor of less than 0.8. Both points put ω_2 at the correct position of $3\omega_1$. However, the desired X-factor should be chosen based on the magnitude ratio $\mathrm{R}_{p2}/\mathrm{R}_{p1}$ of the tank input impedance at resonance. The sum of the even orders of the denominator in (3.4) is zero at resonant frequencies. It can be shown that the first-order terms of the numerator and the denominator are dominant at ω_1. By using (3.6), assuming $Q_p = L_p\omega/r_p$, $Q_s = L_s\omega/r_s$, the tank input impedance at the fundamental frequency is expressed as

$$R_{p1} \approx \frac{L_p}{\omega_1\left(\frac{L_pC_1}{Q_p} + \frac{L_sC_2}{Q_s}\right)} \xRightarrow{Q_p=Q_s=Q_0} R_{p1} \approx L_p\omega_1 Q_0. \tag{3.9}$$

On the other hand, it can be shown that the third-order terms of the numerator and the denominator are dominant in (3.4) at $\omega_2 = 3\omega_1$. It follows that

$$R_{p2} \approx \frac{\left(1-k_m^2\right)}{C_1\omega_2\left(\frac{1}{Q_p} + \frac{1}{Q_s}\right)} \xRightarrow{Q_p=Q_s=Q_0} R_{p2} \approx \frac{Q_0\left(1-k_m^2\right)}{2\,C_1\,\omega_2}. \tag{3.10}$$

R_{p2} is a strong function of the coupling factor of the transformer and thus the resulting leakage inductance. Weaker magnetic coupling will result in higher impedance magnitude at ω_2 and, consequently, the second resonance needs a lower transconductance gain to excite. It could even become a dominant pole and the circuit would oscillate at ω_2 instead of ω_1. This phenomenon has been used to extend the oscillator tuning range in [17, 19], and [20]. As explained before, $\mathrm{R}_{p2}/\mathrm{R}_{p1}$ controls the amount of the third harmonic component of the oscillation voltage. The impedance magnitude ratio is equal to

$$\frac{R_{p2}}{R_{p1}} \approx \frac{\left(1-k_m^2\right)(1+X)}{6}. \tag{3.11}$$

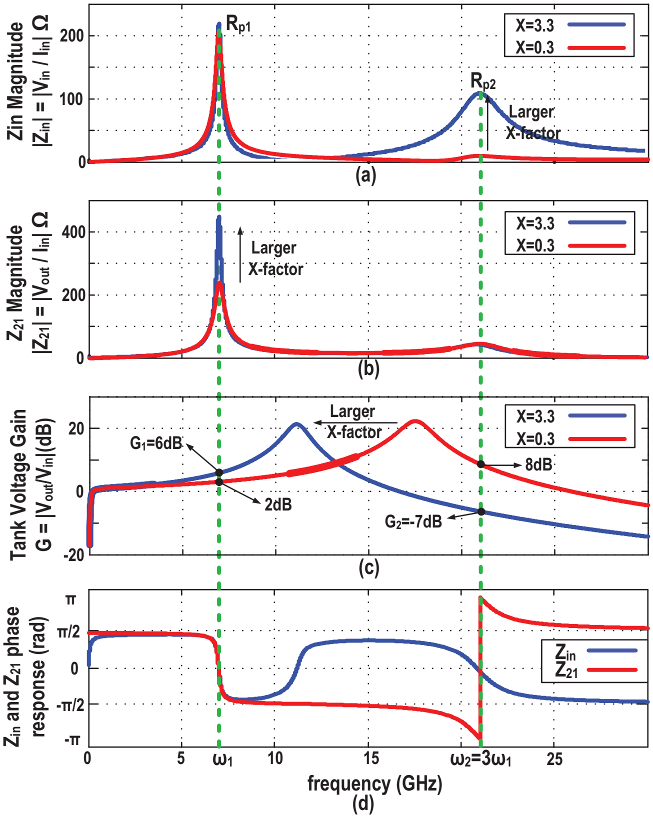

Figure 3.8 The transformer-based tank characteristics: (a) the input impedance, Z_{in} magnitude; (b) the trans-impedance, Z_{21} magnitude; (C) transformer's secondary to primary voltage gain; (d) the phase of Z_{in} and Z_{21} (momentum simulation).

Hence, the smaller X-factor results in lower tank equivalent resistance at $\omega_2 = 3\omega_1$. Thus, the tank filters out more of the third harmonic of the drain current and the oscillation voltage becomes more sinusoidal. Figure 3.8(a) illustrates momentum simulation results of Z_{in} of the transformer-based tank versus frequency for both X-factors that satisfy the resonant frequency ratio of 3. The larger X-factor offers significantly higher tank impedance at ω_2, which is entirely in agreement with the theoretical analysis.

The X-factor is defined as a product of the transformer inductance ratio L_s/L_p and tuning capacitance ratio C_2/C_1. This leads to a question of how to best divide X-factor between the inductance and capacitance ratios. In general, larger L_s/L_p results in higher inter-winding voltage gain, which translates to sharper transition at zero-crossings and larger oscillation amplitude at the secondary winding. Both of these effects have a direct consequence on the phase noise improvement. However, the transformer Q-factor drops by increasing the turns ratio. In addition, very large oscillation voltage swing brings up reliability issues due to the gate-oxide breakdown. It turns out that the turns ratio of 2 can satisfy the aforementioned constraints altogether.

3.2.3 Voltage Gain of the Tank

The transformer-based resonator, whose schematic was shown in Figure 3.6, offers a filtering function on the signal path from the primary to the secondary windings. The tank voltage gain is derived as

$$G(s) = \frac{V_{out}}{V_{in}} = \frac{Ms}{s^3(L_pL_sC_2(1-k_m^2))+s^2(C_2(L_sr_p+L_pr_s))+s(L_p+r_sr_pC_2))+r_p}. \tag{3.12}$$

Bode diagram of the tank voltage gain transfer function is shown in Figure 3.9. The tank exhibits a 20 dB/dec attenuation for frequencies lower than the first pole and offers a constant voltage gain at frequencies between the first pole and the complex conjugate pole pair at ω_p. The gain plot reveals an interesting peak at frequencies around ω_p, beyond which the filter gain drops at the -40 dB/dec slope. The low frequency pole is estimated by

$$\omega_{p1} = \frac{r_p}{L_p}. \tag{3.13}$$

By substituting $r_p = L_p\omega/Q_p$, $r_s = L_s\omega/Q_s$ and assuming $Q_p \cdot Q_s \gg 1$, the tank gain transfer function can be simplified to the following equation for

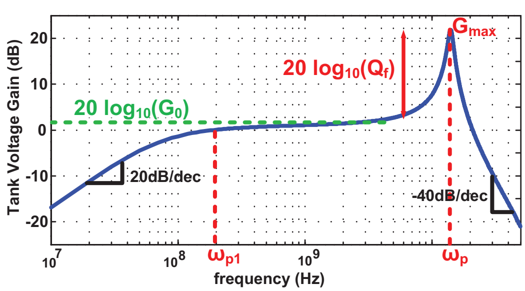

Figure 3.9 Typical secondary-to-primary winding voltage gain of the transformer-based resonator versus frequency.

the frequencies beyond ω_{p1}:

$$G\left(s\right)=\frac{\frac{M}{L_p}}{s^2\left(L_sC_2\left(1-k_m^2\right)\right)+s\left(L_sC_2\omega\left(\frac{1}{Q_p}+\frac{1}{Q_s}\right)\right)+1}. \tag{3.14}$$

The main characteristics of the tank voltage gain can be specified by considering it as a biquad filter.

$$G\left(s\right)=\frac{G_0}{\left(\frac{s}{\omega_p}\right)^2+\left(\frac{s}{\omega_pQ_f}\right)+1}, \tag{3.15}$$

where

$$G_0=k_mn. \tag{3.16}$$

The peak frequency is estimated by

$$\omega_p=\sqrt{\frac{1}{L_sC_2\left(1-k_m^2\right)}} \tag{3.17}$$

Q_f represents the amount of gain jump around ω_p and expressed by

$$Q_f=\frac{\left(1-k_m^2\right)}{\frac{1}{Q_p}+\frac{1}{Q_s}}. \tag{3.18}$$

Hence, the maximum voltage gain is calculated by

$$G_{max}=k_mn\times\frac{\left(1-k_m^2\right)}{\frac{1}{Q_p}+\frac{1}{Q_s}}. \tag{3.19}$$

Equation (3.19) and Figure 3.9 demonstrate that the transformer-based resonator can offer the voltage gain above k_mn at the frequencies near ω_p for $k_m<1$ and the peak magnitude is increased by improving Q-factor of the transformer individual inductors. Consequently, ω_1 should be close to ω_p to have higher passive gain at the fundamental frequency and more attenuation at its harmonic components. Equations (3.6) and (3.17) indicate that ω_p is always located at frequencies above ω_1 and the frequency gap between them decreases with greater X-factor. Figure 3.8(c) illustrates the voltage gain of the transformer-based tank for two different X-factors that exhibit the same resonant frequencies. The transformer peak gain happens at much higher

Table 3.1 Normalized zero-crossing slope of the novel oscillator

	Normalized Zero-crossing Slope
Traditional LC	1
Novel tank (primary)	$1 + 3\zeta = 1 + 3 \cdot 1/6 = 1.5$
Novel tank (secondary)	G_1-$3G_2\zeta = 2.1 - 3 \cdot 0.4 \cdot 1/6 = 1.9$

frequencies for the smaller X-factor and, therefore, the gain is limited to only $k_m n$ (2 dB in this case) at ω_1. However, X-factor is around 3 for the new oscillator and, as a consequence, ω_p moves lower and much closer to ω_1. Now, the tank offers higher voltage gain ($G_1 = 6$ dB in this case) at the main resonance and more attenuation ($G_2 = -7$ dB) at ω_2. This former translates to larger oscillation voltage swing and thus better phase noise.

As can be seen in Figure 3.8(d), the input impedance Z_{in} phase is zero at the first and second resonant frequencies. Hence, any injected third harmonic current has a constructive effect resulting in sharper zero-crossings and flat peak for the transformer's primary winding voltage. However, the tank trans-impedance, Z_{21} phase shows a 180 degree phase difference at ω_1 and $\omega_2 = 3\omega_1$. Consequently, the third harmonic current injection at the primary windings leads to a slower zero-crossings slope at the transformer's secondary, which has an adverse outcome on the phase noise performance of the oscillator. Figure 3.8(a–c) illustrates that this transformer-based resonator effectively filters out the third harmonic component of the drain current at the secondary winding in order to minimize these side effects and zero-crossings are sharpened by tank's voltage gain (G_1) at ω_1. Table 3.1 shows that the zero-crossing slope of this oscillator at both transformer's windings are improved compared to the traditional oscillator for the same V_{DD}, which is translated to shorter commutating time and lower active device noise factor.

3.2.4 Class-F_3 Oscillator

The desired tank impedance, inductance, and capacitance ratios were determined above to enforce the pseudo-square-wave oscillation voltage around the tank. Now, two transistors should be customarily added to the transformer-based resonator to sustain the oscillation. There are two options, however, as shown in Figure 3.10, for connecting the transformer to the active gm-devices. The first option is a transformer-coupled class-F_3 oscillator in which the secondary winding is connected to the gate of the gm-devices. The second option is a cross-coupled class-F_3 oscillator with a floating secondary transformer winding, which only physically connects to tuning capacitors C_2.

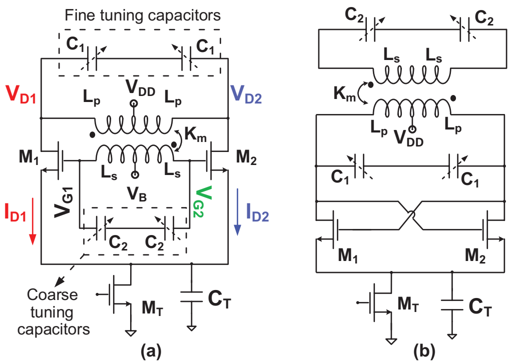

Figure 3.10 Two options of the transformer-based class-F_3 oscillator: (a) transformer-coupled and (b) cross-coupled. The first option was chosen as more advantageous in this work.

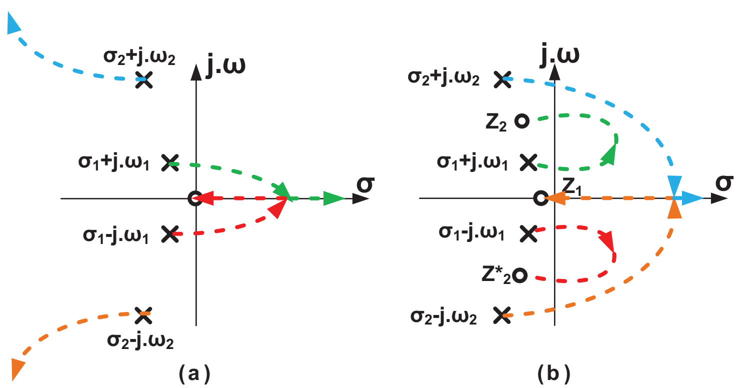

Figure 3.11 Root-locus plot of the transformer-based class-F_3 oscillator: (a) transformer-coupled structure of Figure 3.10(a); and (b) cross-coupled structure of Figure 3.10(b).

The oscillation voltage swing, the equivalent resonator quality factor, and tank input impedance are the same for both options. However, the gm-device sustains larger voltage swing in the first option. Consequently, its commutation time is shorter and the active device noise factor is lower. In addition, the gm-device generates higher amount of the third harmonic, which results in sharper pseudo-square oscillation voltage with lower ISF rms value. The second major difference is about the possibility of oscillation at ω_2 instead of ω_1. The root-locus plot in Figure 3.11 illustrates the route of pole movements towards zeros for different values of the oscillator loop transconductance gain (G_m). As can be seen in Figure 3.11(b), both resonant frequencies (ω_1, ω_2)

can be excited simultaneously with a relatively high value of G_m for the cross-coupled class-F_3 oscillator of Figure 3.10(b). It can increase the likelihood of the undesired oscillation at ω_2. However, the transformer-coupled circuit of Figure 3.10(a) demonstrates a different behavior. The lower frequency conjugate pole pair moves into the right-hand plane by increasing the absolute value of G_m, while the higher poles are pushed far away from imaginary axis (see Figure 3.11(a)). This guarantees that the oscillation can only happen at ω_1. Consequently, it becomes clear that the transformer-coupled oscillator is a better option due to its phase noise performance and the guaranty of operation at the right resonant frequency. Nevertheless, the gate parasitic capacitance appears at the drain through a scaling factor of n^2, which reduces its tuning range somewhat as compared to the cross-coupled candidate.

Figure 3.12(a) illustrates the unconventional oscillation voltage waveforms of this transformer-coupled class-F_3 oscillator. As specified in Section 3.2.3, the third harmonic component of the drain voltage attenuates at the gate and thus a sinusoidal wave is seen there. The gate–drain voltage swing goes as high as $2.7{\cdot}V_{DD}$ due to the significant voltage gain of the tank. Hence, using thick-oxide gm-devices is a constraint to satisfy the time-dependent dielectric breakdown (TDDB) issue for less than 0.01% failure rate during 10 years of the oscillator operation [21, 22]. The costs are larger parasitics capacitance and slightly lower frequency tuning range.

The frequency tuning requires a bit different consideration in the class-F_3 oscillator. Both C_1 and C_2 must, at a coarse level, be changed simultaneously to maintain L_sC_2/L_pC_1 ratio such that ω_2 aligns with $3\omega_1$.

Figure 3.12(b) shows the transient response of the class-F oscillator. At power up, the oscillation voltage is very small and the drain current pulses have narrow and tall shape. Even though the tank has an additional impedance

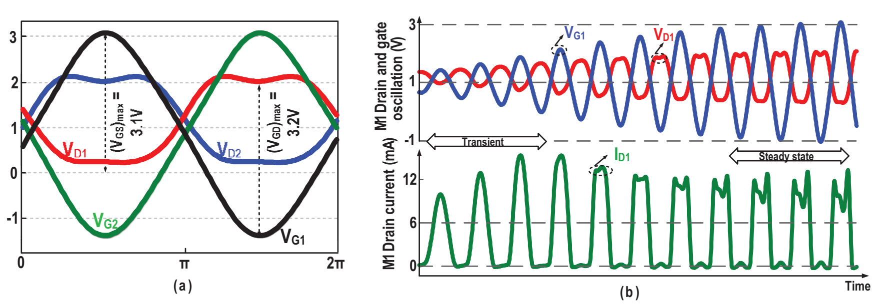

Figure 3.12 (a) Oscillation voltage waveforms and (b) transient response of the class-F_3 oscillator.

at $3\omega_1$, the third harmonic component of the drain current is negligible and, consequently, the drain oscillation resembles a sinusoid. At steady state, gate oscillation voltage swing is large and the gm-device drain current is square wave. Consequently, the combination of the tank input impedance with significant drain's third harmonic component results in the pseudo-square-wave for the drain oscillation voltage. This justifies its "class-F_3" designation.

3.3 Class-F_3 Phase Noise Performance

3.3.1 Quality Factor of Transformer-Based Resonator

The Q-factor of the complex tank, which comprises two coupled resonators, does not appear to be as straightforward in intuitive understanding as the Q-factor of the individual physical inductors. It is, therefore, imperative to understand the relationship between the open-loop Q-factor of the tank versus the Q-factor of the inductive and capacitive parts of the resonator.

First, suppose the tuning capacitance losses are negligible. Consequently, the oscillator equivalent Q-factor just includes the tank's inductive part losses. The open-loop Q-factor of the oscillator is defined as $\omega_0/2 \cdot d\phi/d\omega$, where ω_0 is the resonant frequency and $d\phi/d\omega$ denotes the slope of the phase of the oscillator open-loop transfer function [23]. To determine the open-loop Q, we need to break the oscillator loop at the gate of M_1, as shown in Figure 3.13. The open-loop transfer function is thus given by

$$H(s) = \frac{V_{out}}{I_{in}} = \frac{Ms}{As^4 + Bs^3 + Cs^2 + Ds + 1}, \tag{3.20}$$

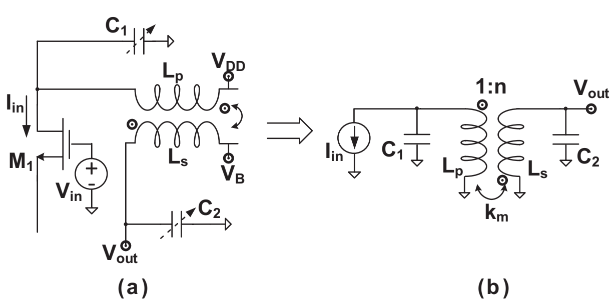

Figure 3.13 Open-loop circuit for unloaded Q-factor calculation (a); its equivalent circuit (b).

where $A = L_pL_sC_1C_2\left(1 - k_m^2\right)$, $B = C_1C_2\left(L_sr_p + L_pr_s\right)$, $C = L_pC_1 + L_sC_2 + r_pr_sC_1C_2$, and $D = r_pC_1 + r_sC_2$. After carrying out lengthy algebra and considering $(1 - C\omega^2 + A\omega^4 \approx 0)$ at the resonant frequencies,

$$Q_i = -\frac{\omega}{2}\frac{d\phi(\omega)}{d\omega} = \frac{\left(C\omega - 2A\omega^3\right)}{\left(D - B\omega^2\right)}. \tag{3.21}$$

Substituting A, B, C, and D into (3.21), then swapping r$_p$ and r$_s$ with $L_p\omega/Q_p$ and $L_s\omega/Q_s$, respectively, and assuming $Q_pQ_s \gg 1$, we obtain

$$Q_i = \frac{\left(L_pC_1 + L_sC_2\right) - 2\left(L_pL_sC_1C_2\left(1 - k_m^2\right)\right)\omega^2}{\left(\frac{L_pC_1}{Q_p} + \frac{L_sC_2}{Q_s}\right) - \left(C_1C_2L_sL_p\left(\frac{1}{Q_p} + \frac{1}{Q_s}\right)\right)\omega^2}. \tag{3.22}$$

Substituting (3.5) as ω into the above equation and carrying out the mathematics, the tank's inductive part Q-factor at the main resonance is

$$Q_i = \frac{\left(1 + X^2 + 2k_mX\right)}{\left(\frac{1}{Q_p} + \frac{X^2}{Q_s}\right)}. \tag{3.23}$$

To help with an intuitive understanding, let us consider a boundary case. Suppose that C$_2$ is negligible. Therefore, X-factor is zero and (3.23) predicts that the Q$_i$ equals to Q$_p$. This is not surprising because no energy would be stored at the transformer's secondary winding and its Q-factor would not have any contribution to the equivalent Q-factor of the tank. In addition, (3.23) predicts that the equivalent Q-factor of the tank's inductive part can exceed Q-factors of the individual inductors. This clearly proves Q-factor enhancement over that of the transformer's individual inductors. The maximum tank's inductive part Q-factor is obtained at the following X-factor for a given k_m, Q$_p$, and Q$_s$.

$$X_{Qmax} = \frac{Q_s}{Q_p}. \tag{3.24}$$

For a typical case of $Q_s = Q_p = Q_0$, the maximum Q$_i$ at ω_1 is calculated by

$$X_{Qi,max} = 1 \rightarrow Q_{i,max} = Q_0\left(1 + k_m\right). \tag{3.25}$$

The above equation indicates that the equivalent Q-factor of the inductive part of the transformer-based resonator can be enhanced by a factor of $1 + k_m$ at the optimum state. However, it does not necessarily mean that the Q-factor of the transformer-based tank generally is superior to the simple LC resonator. The reason is that it is not possible to optimize the Q-factor of both windings of a 1:n transformer at a given frequency and one needs to use lower metal layers for the transformer cross connections, which results in more losses and lower Q-factor [24, 25]. For this prototype, the X-factor is around 3 with $k_m = 0.7$ and the simulated Q_p and Q_s are 14 and 20, respectively. Based on (3.23), the equivalent Q-factor of the inductive part of the tank would be about 26, which is higher than that of the transformers' individual inductors. The Q-factor of the switched capacitance largely depends on the tuning range (TR) and operating frequency of the oscillator and is about 42 for the TR of 25% at 7 GHz resulting in an average Q-factor of 16 for the tank in this design.

3.3.2 Phase Noise Mechanism in Class-F_3 Oscillator

According to the linear time-variant model [14], the phase noise of the oscillator at an offset frequency $\Delta\omega$ from its fundamental frequency is expressed as

$$L(\Delta\omega) = 10\log_{10}\left(\frac{\sum_i N_{L,i}}{2\, q_{max}^2\, (\Delta\omega)^2}\right), \tag{3.26}$$

where q_{max} is the maximum charge displacement across the tuning capacitor C and $N_{L,i}$ is the effective noise produced by ith device given by

$$N_{L,i} = \frac{1}{2\pi N^2}\int_0^{2\pi} \Gamma_i^2(t)\, \overline{i_{n,i}^2(t)} dt \tag{3.27}$$

where $\overline{i_{n,i}^2(t)}$ is the white current noise power density of the ith noise source, Γ_i is its relevant ISF function from the corresponding ith device noise, and N is the number of resonators in the oscillator. N is considered one for single-ended and two for differential oscillator topologies with a single LC tank [7].

Figure 3.14 illustrates the major noise sources of CMOS class-B, class C, and class-F_3 oscillators. R_p and $G_{ds1,2}(t)$ represent the equivalent tank parallel resistance and channel conductance of the gm transistors, respectively. On the other hand, $G_{m1,2}$ and G_{mT} model the noise due to transconductance gain of active core and current source transistors, respectively. By substituting (3.27) into (3.26) and carrying out algebra, the phase noise equation is simplified to

$$L(\Delta\omega) = 10\log_{10}\left(\frac{K_B\, T\, R_p}{2\, Q_t^2\, V_p^2}\cdot F\cdot\left(\frac{\omega_0}{\Delta\omega}\right)^2\right), \tag{3.28}$$

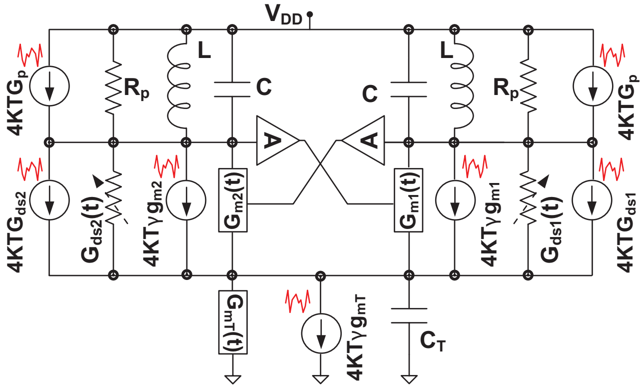

Figure 3.14 RF CMOS oscillator noise sources.

where Q_t is the tank's equivalent quality factor and V_p is the maximum oscillation voltage amplitude, derived by

$$V_p = \begin{cases} \left(\frac{1}{3} + \zeta\right) \sqrt{(1 + \frac{1}{3\zeta}) \cdot \alpha_I \cdot R_p \cdot I_B}, & \frac{1}{9} \leq \zeta \leq 1 \\ (1 - \zeta) \cdot \alpha_I \cdot R_p \cdot I_B, & 0 \leq \zeta \leq \frac{1}{9}, \end{cases} \tag{3.29}$$

where α_I is the current conversion efficiency of the oscillator, expressed as the ratio of the fundamental component of gm-devices drain current to dc current I_B of the oscillator. F in (3.28) is the effective noise factor of the oscillator, expressed by

$$F = \sum_i \frac{1}{2\pi} \int_0^{2\pi} \Gamma_i^2(t) \frac{\overline{i_{n,i}^2(t)} R_p}{4K_B T} dt. \tag{3.30}$$

Suppose that C_T is large enough to filter out the thermal noise of the tail transistor. Consequently, F consists of the noise factor of the tank (F_{tank}), transistor channel conductance (F_{GDS}), and gm of core devices (F_{GM}). The expressions of F_{tank} and F_{GDS} are

$$F_{tank} = \frac{1}{\pi} \int_0^{2\pi} \Gamma_{tank}^2(t) dt = 2\Gamma_{rms}^2 \approx \frac{1 + 9\zeta^2}{(1 + 3\zeta)^2} \tag{3.31}$$

$$F_{GDS} = \frac{1}{\pi} \int_0^{2\pi} \Gamma_{MOS}^2(t) G_{DS1}(t) R_P dt \approx 2\Gamma_{rms}^2 R_P \cdot G_{DS1EF}, \tag{3.32}$$

where G_{DSEF1} is the effective drain–source conductance of one of the gm-devices expressed by

$$G_{DS1EF} = G_{DS1}[0] - G_{DS1}[2], \tag{3.33}$$

where G_{DS1}[k] describes the kth Fourier coefficient of the instantaneous conductance, G_{ds1}(t) [26]. F_{GM} can be calculated by

$$F_{GM} = \frac{1}{\pi}\int_0^{2\pi} \Gamma^2_{MOS}(t)\gamma G_{m1}(t) R_P dt \approx 2\Gamma^2_{rms} \cdot \gamma \cdot R_P \cdot G_{M1EF}. \tag{3.34}$$

Now, the effective negative transconductance of the oscillator needs to overcome the tank and its own channel resistance losses and, therefore, the noise due to G_M also increases.

$$G_{M1EF} = \frac{1}{A}\left(\frac{1}{R_p} + G_{DS1EF}\right), \tag{3.35}$$

where A is the voltage gain of feedback path between the tank and MOS gate. By substituting (3.35) into (3.34)

$$F_{GM} = 2\,\Gamma^2_{rms} \cdot \frac{\gamma}{A} \cdot (1 + R_P G_{DS1EF})\,. \tag{3.36}$$

Consequently, the effective noise factor of the oscillator is given by

$$F = 2\,\Gamma^2_{rms} \cdot \left(1 + \frac{\gamma}{A}\right) \cdot (1 + R_P G_{DS1EF})\,. \tag{3.37}$$

This is a general result and is applicable to the class-B, class-C, and class-F_3. The oscillator FoM normalizes the phase noise performance to the oscillation frequency and power consumption, yielding

$$FoM = -10 \cdot log_{10}\left(\frac{10^3\, K_B\, T}{2\, Q_t^2\, \alpha_I\, \alpha_V} \cdot 2\,\Gamma^2_{rms} \cdot \left(1 + \frac{\gamma}{A}\right) \cdot (1 + R_P G_{DS1EF})\right), \tag{3.38}$$

where α_V is the voltage efficiency, defined as V_P/V_{DD}.

To get a better insight, the circuit-to-phase-noise mechanism, relative phase noise, and power efficiency of different oscillator classes are also investigated and compared together in this section. Figure 3.15(a–f) shows the oscillation voltage and drain current for the traditional, class-C and class-F oscillators for the same V_{DD} (i.e., 1.2 V), tank Q-factor (i.e., 15), and R_P (i.e., 220 Ω).

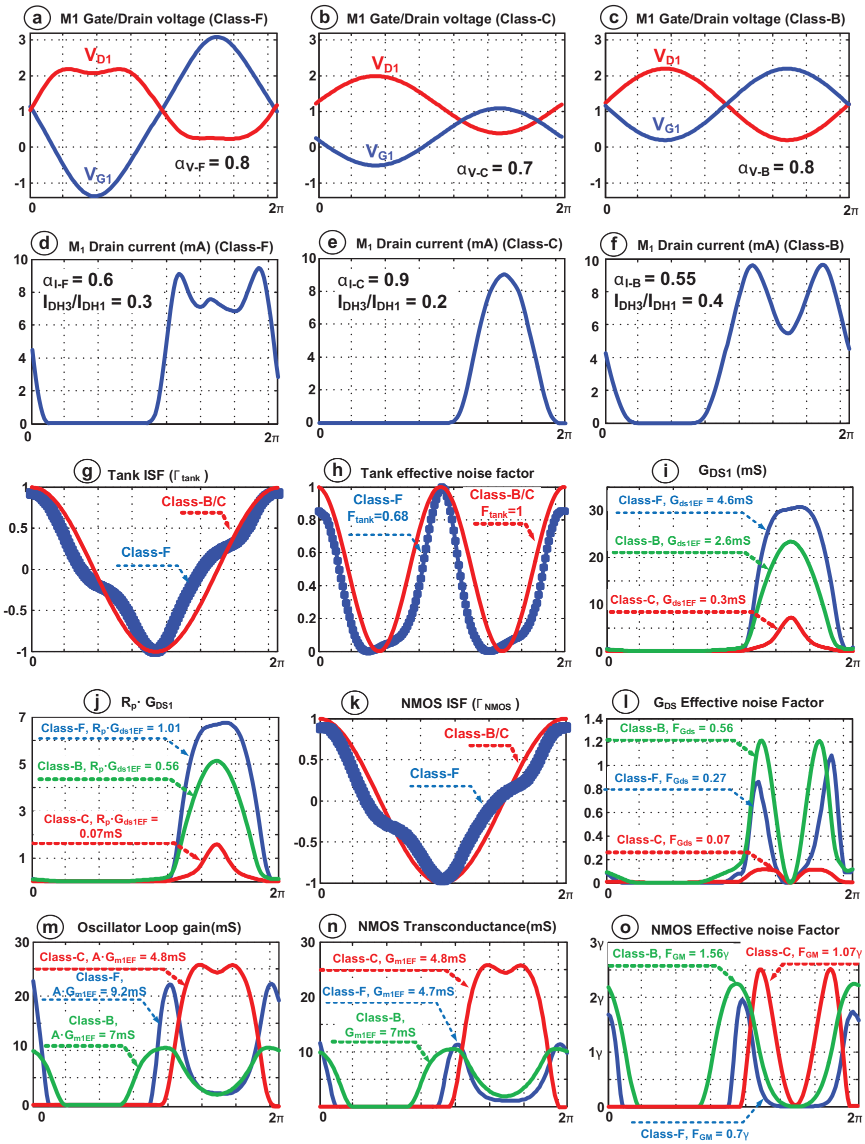

Figure 3.15 Mechanisms of circuit noise to phase noise conversion in different classes of RF CMOS oscillator.

The α_V must be around 0.8 for the class-B and class-F_3 oscillators due to the voltage drop V_{dsat} across the tail transistor needed to keep it in saturation. The combination of the tail capacitance and entering the gm-devices into the linear region reduces α_I of class-B from the theoretical value of $2/\pi$ to around 0.55. Fortunately, α_I is maintained around $2/\pi$ for class-F_3 due to the pseudo-square drain voltage and larger gate amplitude. The class-C oscillator with a dynamic bias of the active transistor offers significant improvements over the traditional class-C and maximizes the oscillation amplitude without compromising the robustness of the oscillator start-up [27]. Nevertheless, its α_V is around 0.7 to avoid gm-devices entering the triode region. Class-C drain current composed of tall and narrow pulses results in α_I equal to 0.9 (ideally 1).

Obtaining the ISF function is the first step in the calculation of the oscillator's effective noise factor. The class-B/C ISF function is a sinusoid in quadrature with the tank voltage [7, 28]. However, finding the exact equation of class-F_3 ISF is not possible; hence, we had to resort to painstakingly long Cadence^{TM} simulations to obtain the ISF curves. Figure 3.15(g) shows the simulated class-F tank equivalent ISF function, which is smaller than the other classes for almost the entire oscillation period.

Figure 3.15(h) demonstrates the tank effective noise factor along the oscillation period for different oscillator classes. The F_{RP} is 32% lower for this class-F_3 due to its special ISF properties. The gm-device M_1 channel conductance across the oscillation period is shown in Figure 3.15(i). As expected, $G_{DS1}(t)$ of class-F_3 exhibits the largest peak due to high oscillation swing at the gate and, consequently, injects more noise than other structures to the tank. On the other hand, class-C operates only in the saturation region and its effective transistor conductance is negligible. Figure 3.15(j) strongly emphasizes that the gm-device resistive channel noise could even be 7 times higher than the tank noise when the M_1 operates in the linear region. To get a better insight, one need to simultaneously focus on Figures 3.15(j) and (k). Although the class-F_3 G_{DS1} generates lots of noise in the second half of the period, its relevant ISF value is very small there. Hence, the excessive transistor channel noise cannot convert to the phase noise and as shown in Figure 3.15(l), the F_{GDS} of class-F_3 is one-half of the traditional oscillator. The transconductance loop gains of the different oscillator structures are shown in Figure 3.15(m). Class-F_3 needs to exhibit the highest effective transconductance loop gain to compensate its larger gm-devices channel resistance losses. However, half of the required loop gain is covered by the transformer-based tank voltage gain. Figure 3.15(o) demonstrates the active device effective noise factor along the oscillation period. Class-F_3 offers the lowest F_{GM} due to its special ISF nature and the passive voltage gain between the tank and gate of the gm-transistors.

Table 3.2 Comparison of different oscillator's classes for the same V_{DD} (1.2 V), tank Q-factor (15), R_P (i.e. 220 Ω), and carrier frequency (7 GHz) at 3 MHz offset frequency

	Theoretical Expression	Class-B	Class-C	Class-F$_3$
F_{RP}	$2\Gamma^2_{rms}$	1 (average)	1 (average)	0.7 (best)
F_{GDS}	$2\Gamma^2_{rms} R_P G_{DSEF1}$	0.56 (worst)	0.07 (best)	0.27 (average)
F_{GM}	$2\Gamma^2_{rms} \frac{\gamma}{A} \left(1 + R_P G_{DS1EF}\right)$	1.56γ (worst)	1.07γ (average)	0.7γ (best)
F	$2\,\Gamma^2_{rms}\left(1 + \frac{\gamma}{A}\right)\left(1 + R_P G_{DS1EF}\right)$	5.5 dB (worst)	3.9 dB (average)	2.8 dB (best)
α_I	I_{H1}/I_B	0.55 (worst)	0.9 (best)	0.63 (average)
α_V	V_p/V_{DD}	0.8 (best)	0.7 (average)	0.8 (best)
$PN(dBc/Hz)$	$10\log_{10}\left(\frac{K_B\,T\,R_p}{2\,Q_0^2\,V_p^2}\cdot F\cdot\left(\frac{\omega_0}{\Delta\omega}\right)^2\right)$	−133.5 (worst)	−134 (average)	−136 (best)
$FoM\ (dB)$	$-10\log_{10}\left(\frac{1000\,K_B T}{2Q_0^2\alpha_I\alpha_V}F\right)$	191.2 (worst)	194.5 (best)	194.2 (≈ best)

Table 3.2 summarizes the performance of different oscillator classes of this example. It can be concluded that class-F$_3$ oscillator achieves the lowest circuit-to-phase-noise conversion along the best phase noise performance with almost the same power efficiency as the class-C oscillator.

The use of transformer in the class-F$_3$ configuration offers an additional reduction of the 1/f^3 phase noise corner. The transformer inherently rejects the common-mode signals. Hence, the 1/f noise of the tail current source can appear at the transformer's primary, but it will be effectively filtered out on the path to the secondary winding. Consequently, the AM-to-PM conversion at the C_2 switched capacitors is entirely avoided.

3.3.3 Class-F$_3$ Operation Robustness

Figure 3.16(a) illustrates the tank input impedance magnitude and phase for the imperfect position of the second resonance frequency ω_2. A 6% mismatch is applied to the C_2/C_1 ratio, which shifts ω_2 to frequencies higher than $3\omega_1$. Hence, the third harmonic of the drain current is multiplied by a lower impedance magnitude with a phase shift resulting in a distorted pseudo-square oscillation waveform as shown in Figure 3.16(b). Intuitively, if the Q-factor at ω_2 was smaller, the tank impedance bandwidth around it would be wider. Therefore, the tank input impedance phase shift and magnitude reduction would be less for a given ω_2 drift from $3\omega_1$. As a consequence, the oscillator would be less sensitive to the position of ω_2 and thus the tuning capacitance ratio. Based on the open-loop Q-factor analysis, substituting $\omega^2 \approx 9/(L_sC_2 + L_pC_1)$ into (3.22), the Q_i is obtained as $0.3Q_0$ at ω_2. Fortunately enough, the proposed tank configuration automatically reduces

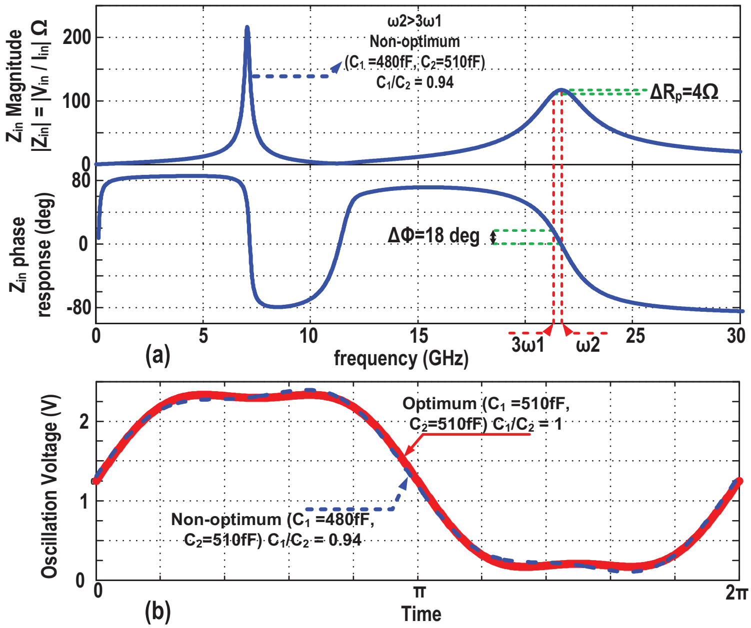

Figure 3.16 Sensitivity of class-F_3 oscillator to the position of the second resonant frequency: tank's input impedance magnitude and phase (top); oscillation waveform (bottom).

the equivalent tank Q-factor at ω_2 to 30% of the main resonance Q-factor. This is completely in line with the desire to reduce the sensitivity to the position of ω_2 in class-F_3. Consequently, a realistic example ± 30 fF variation in C_1 from its optimum point has absolutely no major side effects on the oscillator waveform and thus its phase noise performance, as apparent from Figure 3.16. It is strongly emphasized that the circuit oscillates based on ω_1 resonance, and low Q-factor at ω_2 has no adverse consequence on the oscillator phase noise performance.

3.4 Experimental Results

3.4.1 Implementation Details

The class-F_3 oscillator, whose schematic was shown in Figure 3.10(a), has been realized in TSMC 1P7M 65-nm CMOS technology with Alucap layer. The differential transistors are thick-oxide devices of 12(4-µm/0.28-µm) dimension to withstand large gate voltage swing. However, the tail current source M_T is implemented as a thin-oxide 500-µm/0.24-µm device biased in saturation. The large channel length is selected to minimize its 1/f noise. Its large drain–bulk and drain–gate parasitic capacitances combined with $C_T = 2$ pF MOM capacitor shunt the M_T thermal noise to ground. The step-up 1:2 transformer is realized by stacking the 1.45 μm Alucap layer on top of the 3.4 μm thick top (M7 layer) copper metal. Its primary and secondary differential self-inductances are about 500 and 1500 pH, respectively, with the magnetic coupling factor of 0.73. The transformer was designed with a goal of maximizing Q-factor of the secondary winding, Q_s, at the desired operating frequency. Based on (3.23), Q_s is the dominant factor in the tank equivalent Q-factor expression, provided $(L_s C_2)/(L_p C_1)$ is larger than one, which is valid for this oscillator prototype. In addition, the oscillation voltage is sinusoidal across the secondary winding. It means the oscillator phase noise is more sensitive to the circuit noise at the secondary winding compared to the primary side with the pseudo-square waveform. Four switched MOM capacitors $B_{C0} - B_{C3}$ placed across the secondary winding realize coarse tuning bits, while the fine control bits $B_{F0} - B_{F3}$ with LSB size of 20 fF adjust the position of ω_2 near $3\omega_1$. The center tap of the secondary winding is connected to the bias voltage, which is fixed around 1 V to guarantee safe oscillator start-up in all process corners. A resistive shunt buffer interfaces the oscillator output to the dynamic divider [2]. A differential output buffer drives a 50-Ω load. The separation of the oscillator core and divider/output buffer voltage supplies and grounds serves to maximize the isolation between the circuit blocks. The die micrograph is shown in Figure 3.17. The oscillator core die area is 0.12 mm^2.

3.4.2 Measurement Results

The measured phase noise at 3.7 GHz (after the on-chip ÷2 divider) at 1.25 V and 12 mA current consumption is shown in Figure 3.18. The phase noise of −142.2 dBc/Hz at 3 MHz offset lies on the 20 dB/dec slope, which extrapolates to −158.7 dBc/Hz at 20 MHz offset (−170.8 dBc/Hz when normalized to 915 MHz) and meets the GSM TX mobile station (MS) specification with a very wide 8 dB margin. The oscillation purity of the class-F_3 oscillator is good enough to compare its performance to cellular basestation (BTS) phase noise requirements. The GSM/DCS “Micro” BTS phase noise requirements are easily met. However, the phase noise would be off by 3 dB for the toughest DCS-1800 “Normal” BTS specification at 800 kHz offset frequency [29]. The $1/f^3$ phase noise corner is around 700 kHz at the highest frequency due to the asymmetric layout of the oscillator differential nodes further magnified

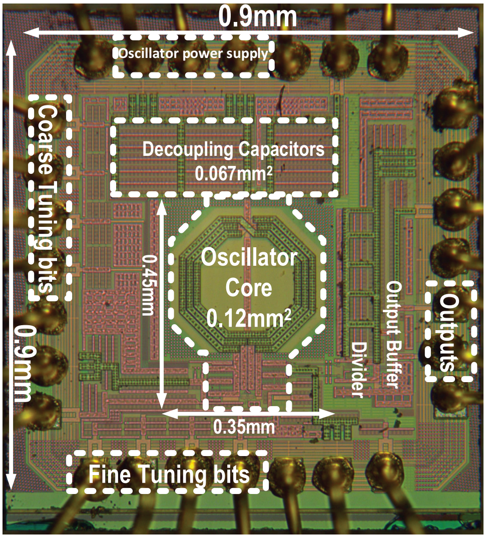

Figure 3.17 Die photograph of class-F3 oscillator.

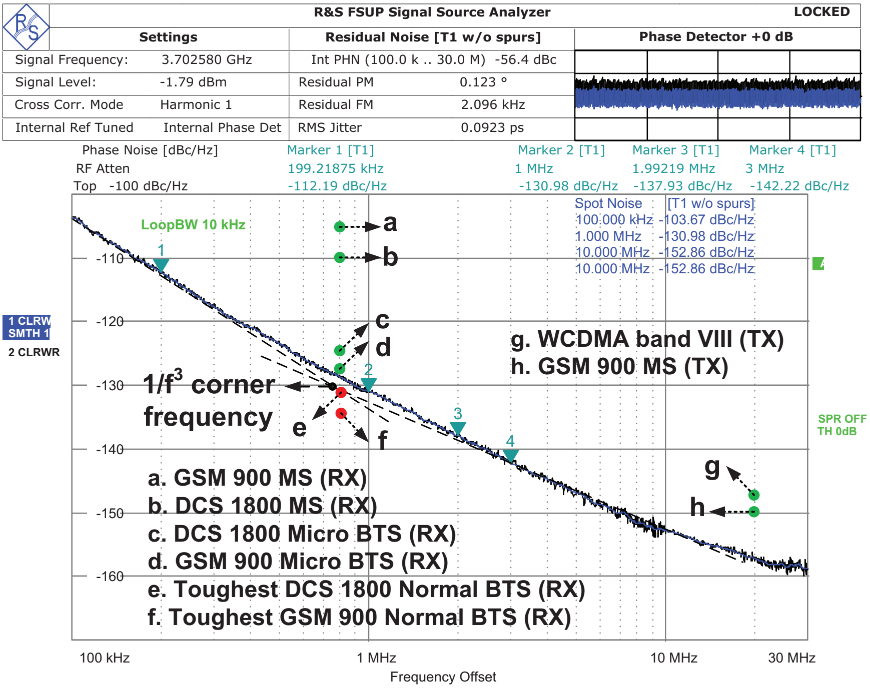

Figure 3.18 Measured phase noise at 3.7 GHz and power dissipation of 15 mW. Specifications (MS: mobile station; BTS: basestation) are normalized to the carrier frequency.

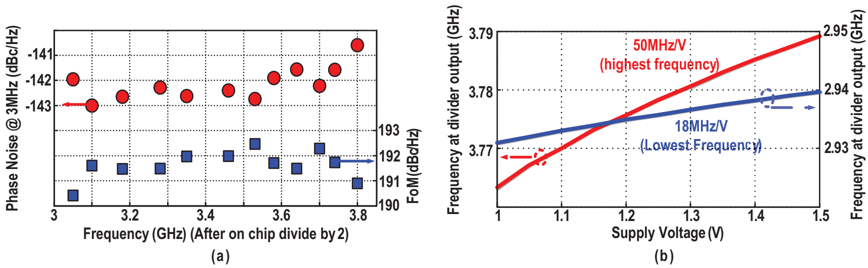

Figure 3.19 (a) Phase noise and figure of merit (FoM) at 3 MHz offset versus carrier frequency and (b) frequency pushing due to supply voltage variation.

by the dominance of parasitics in the equivalent tank capacitance. The 1/f^3 phase noise corner moves to around 300 kHz at the middle and low parts of the tuning range. The noise floor is -160 dBc/Hz and dominated by thermal noise from the divider and buffers. The oscillator has a 25% tuning range from 5.9 to 7.6 GHz. Figure 3.19(a) shows the average phase noise performance of four samples at 3 MHz offset frequency across the tuning range (after the divider), together with the corresponding FoM. The average FoM is as high as 192 dBc/Hz and varies about 2 dB across the tuning range. The divided output frequency versus supply is shown in Figure 3.19(b) and reveals very low frequency pushing of 50 and 18 MHz/V at the highest and lowest frequencies, respectively.

The phase noise of the class-F$_3$ oscillator was measured at the fixed frequency of 3.5 GHz for two configurations. In the first configuration, the C_2/C_1 ratio was set to one to align the second resonant frequency ω_2 exactly at the third harmonic of the fundamental frequency ω_1. This is the optimum configuration of the class-F$_3$ oscillator (Figure 3.20, top). In the second configuration, the oscillation frequency is kept fixed, but an unrealistically high 40% mismatch was applied to the C_2/C_1 ratio, which lowers ω_2, in order to see its effects on the phase noise performance (see Figure 3.20, bottom). As a consequence, the third harmonic component of the drain oscillation voltage is reduced and a phase shift can be seen between voltage waveform components at $3\omega_1$ and ω_1. Therefore, its ISF rms value is worse than optimum, thus causing a 2-dB phase noise degradation in the 20-dB/dec region. In addition, the voltage waveform demonstrates more asymmetry in the rise and fall times, which translates to the non-zero ISF dc value and increases the upconversion factor of the 1/f noise corner of gm-devices. As can be seen in Figure 3.20, the 1/f^3 phase noise corner is increased by 25% or 100 kHz in the non-optimum case. It results in a 3-dB phase noise penalty in the flicker noise region.

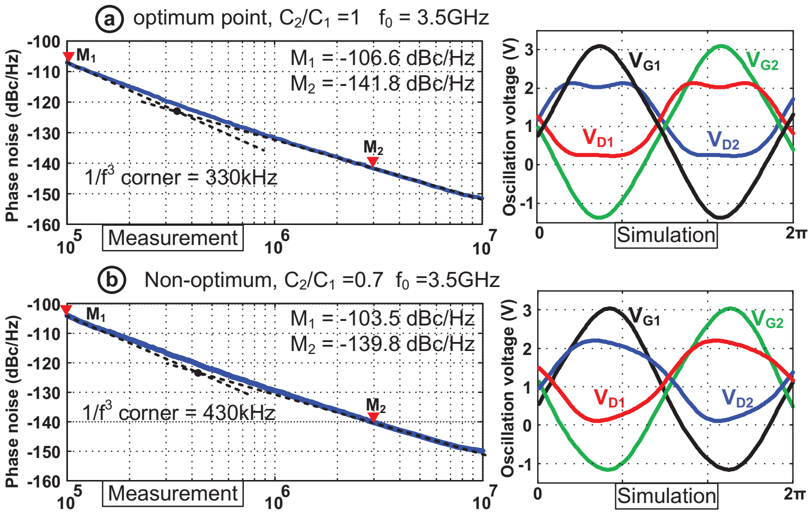

Figure 3.20 Measured phase noise at 3.5 GHz and simulated oscillation waveforms: (a) optimum case; (b) exaggerated non-optimum case.

Table 3.3 summarizes performance of this class-F_3 oscillator and compares it with the relevant oscillators. The class-F_3 demonstrates a 5-dB phase noise and 7-dB FoM improvements over the traditional commercial oscillator [2] with almost the same tuning range. For the same phase noise performance range (-154 to -155 dBc/Hz) at 3-MHz offset for the normalized 915-MHz carrier, the class-F_3 oscillator consumes only 15 mW, which is much lower than that with Colpitts [30], class B/C [10], and clip-and-restore [29] topologies. Only the noise-filtering-technique oscillator [8] offers a better power efficiency but at the cost of an extra dedicated inductor and thus larger die. Also, it uses a 2.5-V supply, thus making it unrealistic in today's scaled CMOS. From the FoM point of view, the class-C oscillator [9] exhibits a better performance than the class-F_3 oscillator. However, the voltage swing constraint in class-C limits its phase noise performance. As can be seen, the class-F_3 demonstrates more than 6 dB better phase noise with almost the same supply voltage. Consequently, the class-F_3 oscillator has reached the best phase noise performance with the highest power efficiency at low voltage supply without the die area penalty of the noise-filtering technique or voltage swing constraint of the class-C VCOs.

Class-F_3 operation is also extended to mm-wave frequency generation in [32] and [33] which may interest a curious reader.

Table 3.3 Comparison with relevant oscillators

	This work	[9]	[8]	[29]	[10]	[30]	[2]	[20]
Technology	CMOS 65 nm	CMOS 130 nm	CMOS 350 μm	CMOS 65 nm	CMOS 55 nm	BiCMOS 0.130 μm	CMOS 90 nm	CMOS 65 nm
Supply voltage (V)	1.25	1	2.5	1.2	1.5	3.3	1.4	0.6
Frequency (GHz)	3.7[1]	5.2	1.2	3.92[1]	3.35[1]	1.56	0.915	3.7
Tuning range (%)	25	14	18	10.2	31.4	9.6	24.3	77
PN at 3 MHz (dBc/Hz)	−142.2	−141.2	−152	−141.7	−142	−150.4	−149	−137.1
Norm. PN[2] (dBc/Hz)	−154.3	−147.5	−154.8	−154.4	−153.3	−155	−149	−149.21
I_{DC} (mA)	12	1.4	3.74	18	12	88	18	17.5
Power consumption (mW)	15	1.4	9.25	25.2	27	290	25.2	10.5
FoM[3] (dB)	192.2	195	195	189.9	189	180	184.6	188.7
FoM_T^4 (dB)	200.2	198.4	200.7	190	199	179.7	192.3	206.5
Inductor/transformer count	1	1	2	2	1	1	1	1
Area (mm^2)	0.14	0.11	N/A	0.19	0.196	N/A	N/A	0.294
Oscillator structure	Class-F_3	Class-C	Noise filtering	Clip-and-restore	Class B/C	Colpitts	Tradi tional	Dual mode

[1] After on-chip ÷2 divider.
[2] Phase noise at 3-MHz offset frequency normalized to 915-MHz carrier.
[3] $FOM = |PN| + 20\log_{10}((f_0/\Delta f)) - 10\log_{10}(P_{DC}/1\text{mW})$.
[4] $FOM_T = |PN| + 20\log_{10}((f_0/\Delta f)(TR/10)) - 10\log_{10}(P_{DC}/1\text{mW})$.

3.5 Conclusion

We showed a LC-tank oscillator structure that introduces an impedance peak around the third harmonic of the oscillating waveform such that the third harmonic of the active device current converts into voltage and, together with the fundamental component, creates a pseudo-square oscillation voltage. The additional peak of the tank impedance is realized with a transformer-based resonator. As a result, the oscillator impulse sensitivity function reduces, thus lowering the conversion sensitivity of phase noise to various noise sources, whose mechanisms are analyzed in depth. Chief of these mechanisms arises when the active g_m-devices periodically enter the triode region during which the LC tank is heavily loaded while its equivalent quality factor is significantly reduced. The voltage gain, relative pole position, impedance magnitude, and equivalent quality factor of the transformer-based resonator are quantified at its two resonant frequencies. The gained insight reveals that the secondary to the primary voltage gain of the transformer can be even larger than its turns ratio. A comprehensive study of circuit-to-phase-noise conversion mechanisms of different oscillators' structures shows that the introduced class-F_3 exhibits the lowest phase noise at the same tank's quality factor and supply voltage. Based on this analysis, a class-F_3 oscillator was prototyped in a 65-nm CMOS technology. The measurement results proved expected performance of this oscillator in silicon.

References

[1] E. Hegazi and A. A. Abidii, "A 17-mW transmitter and frequency synthesizer for 900-MHz GSM fully integrated in 0.35-μm CMOS," *IEEE J. Solid-State Circuits*, vol. 38, no. 5, pp. 782–792, May 2003.

[2] R. B. Staszewski, J. L. Wallberg, S. Rezeq, C.-M. Hung, O. E. Eliezer, S. K. Vemulapalli, C. Fernando, K. Maggio, R. Staszewski, N. Barton, M.-C. Lee, P. Cruise, M. Entezari, K. Muhammad, and D. Leipold, "All-digital PLL and transmitter for mobile phones," *IEEE J. Solid-State Circuits*, vol. 40, no. 12, pp. 2469–2482, Dec. 2005.

[3] L. Vercesi, L. Fanori, F. D. Bernardinis, A. Liscidini, and R. Castello, "A dither-less all digital PLL for cellular transmitters," *IEEE J. Solid-State Circuits*, vol. 47, no. 8, pp. 1908–1920, Aug. 2012.

[4] H. Darabi, P. Chang, H. Jensen, A. Zolfaghari, P. Lettieri, J. C. Leete, B. Mohammadi, J. Chiu, Q. Li, S.-L. Chen, Z. Zhou, M. Vadipour, C. Chen, Y. Chang, A. Mirzaei, A. Yazdi, M. Nariman, A. Hadji-Abdolhamid, E. Chang, B. Zhao, K. Juan, P. Suri, C. Guan, L. Serrano, J. Leung, J. Shin, J. Kim, H. Tran, P. Kilcoyne, H. Vinh, E. Raith, M. Koscal, A. Hukkoo, V. R. C. Hayek, C. Wilcoxson, M. Rofougaran, and A. Rofougaran, "A quad-band GSM/GPRS/EDGE SoC in 65nm CMOS," *IEEE J. Solid-State Circuits*, vol. 46, no. 4, pp. 872–882, Apr. 2011.

[5] J. Borremans, G. Mandal, V. Giannini, B. Debaillie, M. Ingels, T. Sano, B. Verbruggen, and J. Craninckx, "A 40nm CMOS 0.4-6 GHz receiver resilient to out-of-band blockers," *IEEE J. Solid-State Circuits*, vol. 46, no. 7, pp. 1659–1671, Jul. 2011.

[6] J. Rael and A. Abidi, "Physical processes of phase noise in differential LC oscillators," *Proceedings of IEEE Custom Integrated Circuits Conference (CICC)*, 2000, pp. 569–572.

[7] P. Andreani, X. Wang, L. Vandi, and A. Fard, "A study of phase noise in Colpitts and LC-tank CMOS oscillators," *IEEE J. Solid-State Circuits*, vol. 40, no. 5, pp. 1107–1118, May 2005.

[8] E. Hegazi, H. Sjoland, and A. A. Abidi, "A filtering technique to lower LC oscillator phase noise," *IEEE J. Solid-State Circuits*, vol. 36, no. 12, pp. 1921–1930, Dec. 2001.

[9] A. Mazzanti and P. Andreani, "Class-C harmonic CMOS VCOs, with a general result on phase noise," *IEEE J. Solid-State Circuits*, vol. 43, no. 12, pp. 2716–2729, Dec. 2008.

[10] L. Fanori, A. Liscidini, and P. Andreani, "A 6.7-to-9.2 GHz 55 nm CMOS hybrid class-B/class-C cellular TX VCO," *IEEE International Solid-State Circuits Conference Digest of Technical Papers (ISSCC)*, Feb. 2012, pp. 354–355.

[11] H. Kim, S. Ryu, Y. Chung, J. Choi, and B. Kim, "A low phase-noise CMOS VCO with harmonic tuned LC tank," *IEEE Transactions on Microwave Theory and Techniques*, vol. 54, no. 7, pp. 2917–2923, Jul. 2006.

[12] M. Babaie and R. B. Staszewski, "Third-harmonic injection technique applied to a 5.87-to-7.56 GHz 65 nm class-F oscillator with 192 dBc/Hz FoM," *IEEE International Solid-State Circuits Conference Digest of Technical Papers (ISSCC)*, 2013, pp. 348–349.

[13] M. Babaie, and R. B. Staszewski, "A class-F CMOS oscillator," *IEEE J. Solid-State Circuits*, vol. 48, no. 12, pp. 3120–3133, Dec. 2013.

[14] A. Hajimiri and T. H. Lee, "A general theory of phase noise in electrical oscillators," *IEEE J. Solid-State Circuits*, vol. 33, no. 2, pp. 179–194, Feb. 1998.

[15] B. Razavi, "A millimeter-wave circuit technique," *IEEE J. Solid-State Circuits*, vol. 43, no. 9, pp. 2090–2098, Sept. 2008.

[16] J. R. Long, "Monolithic transformers for silicon RF IC design," *IEEE J. Solid-State Circuits*, vol. 35, no. 9, pp. 1368–1382, Sept. 2000.

[17] A. Bevilacqua, F. P. Pavan, C. Sandner, A. Gerosa, and A. Neviani, "Transformer-based dual-mode voltage-controlled oscillators," *IEEE Transactions on Circuits and Systems II, Exp. Briefs*, vol. 54, no. 4, pp. 293–297, Apr. 2007.

[18] A. Geol and H. Hashemi, "Frequency switching in dual-resonance oscillators," *IEEE J. Solid-State Circuits*, vol. 42, no. 3, pp. 571–582, Mar. 2007.

[19] B. Razavi, "Cognitive radio design challenges and techniques," *IEEE J. Solid-State Circuits*, vol. 45, no. 8, pp. 1542–1553, Aug. 2010.

[20] G. Li, L. Liu, Y. Tang, and E. Afshari, "A low-phase-noise wide-tuning-range oscillator based on resonant mode switching," *IEEE J. Solid-State Circuits*, vol. 47, no. 6, pp. 1295–1308, Jun. 2012.

[21] R. Degraeve, J. Ogier, R. Bellens, P. Roussel, G. Groeseneken, and H. Maesi, "A new model for the field dependence of intrinsic and

extrinsic time-dependent dielectric breakdown," *IEEE Transactions on Electron Devices*, vol. 45, no. 2, pp. 472–481, Feb. 2007.

[22] M. Babaie and R. Staszewski, "A Study of RF Oscillator Reliability in Nanoscale CMOS," *European Conference on Circuit Theory and Design (ECCTD)*, Sept. 2013 pp. 1–4.

[23] B. Razavi, "A study of phase noise in CMOS oscillators," *IEEE J. Solid-State Circuits*, vol. 31, no. 3, pp. 331–343, Mar. 1996.

[24] H. Krishnaswamy and H. Hashemi, "Inductor and transformer-based integrated RF oscillators: A comparative study," *Proceedings of IEEE Custom Integrated Circuits Conference (CICC)*, 2006, pp. 381–384.

[25] P. Andreani and J. R. Long, "Misconception regarding of transformer resonators in monolithic oscillator," *Electronic Letter*, vol. 42, no. 7, pp. 387–388, Mar. 2006.

[26] D. Murphy, J. J. Rael, and A. A. Abidi, "Phase noise in LC oscillators: A phasor-based analysis of a general result and of loaded Q," "Transformer-based dual-mode voltage-controlled oscillators," *IEEE Transactions on Circuits and Systems I, Reg. Papers*, vol. 57, no. 6, pp. 1187–1203, Jun. 2010.

[27] L. Fanori and P. Andreani, "Low-phase-noise 3.4–4.5 GHz dynamic bias class-C CMOS VCOs with a FoM of 191 dBc/Hz," *Proceedings of European Solid-state Circuits Conference (ESSCIRC)*, 2012, pp. 406–409.

[28] P. Andreani and A. Fard, "More on the phase noise performance of CMOS differentia lpair LC-tank oscillators," *IEEE J. Solid-State Circuits*, vol. 41, no. 12, pp. 2703–2712, Dec. 2006.

[29] A. Visweswaran, R. B. Staszewski, and J. R. Long, "A clip-and-restore technique for phase desensitization in a 1.2 V 65 nm CMOS oscillator for cellular mobile and base station," *IEEE International Solid-State Circuits Conference Digest of Technical Papers (ISSCC)*, 2012, pp. 350–351.

[30] J. Steinkamp, F. Henkel, P. Waldow, O. Pettersson, C. Hedenas, and B. Medin, "A Colpitts oscillator design for a GSM base station synthesizer," *Proceedings of IEEE Radio Frequency Integrated Circuits (RFIC) Symposium*, 2004, pp. 405–408.

[31] M. Babaie and R. B. Staszewski, "Class-F CMOS oscillator incorporating differntial passive network," *US Patent 9,197,221*, issued 24 Nov. 2015.

[32] Z. Zong, M. Babaie, and R. B. Staszewski, "A 60 GHz frequency generator based on a 20 GHz oscillator and an implicit multiplier," *IEEE*

Journal of Solid-State Circuits (JSSC), vol. 51, no. 5, pp. 1261–1273, May 2016.

[33] Z. Zong, P. Chen, and R. B. Staszewski, “A low-noise fractional-N digital frequency synthesizer with Implicit frequency tripling for mm-wave applications,” *IEEE Journal of Solid-State Circuits (JSSC),* vol. 54, no. 3, pp. 755–767, Mar. 2019.